Ti/TiO$_2$/Cu$_2$O electrodes for photocatalytic applications: Synthesis and characterization

Cite as: AIP Conference Proceedings **2145**, 020005 (2019); https://doi.org/10.1063/1.5123566

Antonio Rubino, Pier Giorgio Schiavi, Pietro Altimari, and Francesca Pagnanelli

AIP Conference Proceedings **2145**, 020005 (2019); https://doi.org/10.1063/1.5123566

Ti/TiO_2/Cu_2O Electrodes for Photocatalytic Applications: Synthesis and Characterization

Antonio Rubino[1, a)], Pier Giorgio Schiavi[1], Pietro Altimari[1], Francesca Pagnanelli[1]

[1] *Department of Chemistry, Sapienza University of Rome, P.le A. Moro 00185 Rome (IT)*

[a)]Corresponding author: antonio.rubino@uniroma1.it

Abstract. Energy from renewables (solar, photovoltaic, geothermal), is a major challenge for researchers' efforts in reason of the intermittent nature of these energy sources. Systems like photoelectrochemical (PEC) cells are promising devices that allow the direct conversion of solar energy into electric power and/or chemical fuels. The direct conversion of solar energy in fuels can be achieved using photocatalysts, based on semiconductors like TiO_2.

In this work TiO_2 nanotubes were achieved through "one-step" anodization of titanium, a low cost and accurate method which allowed to control dimensions and morphology of the nanostructured Ti/TiO_2 electrodes. Central limit for TiO_2 photoconversion efficiency is its wide bandgap (i.e. ~3.2eV), which limits light absorption to the ultraviolet region (3–5% of the solar radiation). Composite Cu_2O/TiO_2 systems have attracted much attention: Cu_2O is a promising semiconductor material (bandgap 2.0-2.6eV), suitable to absorb visible light. Traditionally, Cu_2O deposition techniques include the impregnation of TiO_2 with a copper salt and subsequent calcination, but offers little control on sizes, shape and deposit's composition. In this work we developed an electrodeposition method in order to control Cu_2O morphology and sizes in the composed Ti/TiO_2/Cu_2O electrodes.

INTRODUCTION

The risks arising from global warming have led to increasing attention on the development of energy production systems from renewables (solar, photovoltaic, geothermal) [1]. Central limit is the intermittent nature of these energy sources in addition to the fact that related available storage systems are insufficient to guarantee the autonomy in many applications. A promising strategy to overcome these limits is the energy conversion in chemical fuels, which can be stored and subsequently used to generate power. Between these fuels particular attention is paid to hydrogen (high energy density, null environmental impact) [2]. The direct conversion of solar energy into hydrogen can be achieved using photocatalysts, which are based on semiconductor materials, following two different approaches: photocatalytic water-splitting [3] and photocatalytic "reforming" of organics [4]. Semiconductors employed as photocatalysts are the transition metals oxides, like titanium dioxide (TiO_2) [5], which is one of the most studied mainly for high photocatalytic activity, photochemical stability, non- toxicity and low cost [6]. Central limit for the TiO_2 based systems, besides the rate of recombination of the hole-electron pairs, is related to the wide band gap of this semiconductor which makes it suitable only for UV light absorption, with the consequent absence of photoactivity in the visible region of solar spectrum. To overcome the TiO_2 limit, different strategies have been proposed, such as doping with metal [7] or non-metal [8] atoms, combination with other semiconductors [9] or deposition of noble metal particles on the oxide surface [10]. Composite semiconductor systems like Cu_2O/TiO_2 are being in development to overcome the above mentioned TiO_2 limits. Cu_2O is a semiconductor characterized by a narrow band gap which makes it suitable for visible light absorption, furthermore, considering the energy levels of the conduction bands (CB) of the two semiconductors, TiO_2 CB is the less cathodic and so it may act as "trap" for the electrons photogenerated in Cu_2O slowing down the rate of recombination of the hole-electron pairs [11]. Different techniques have been developed to produce TiO_2, such as sol-gel synthesis [12], anodization [13], electrodeposition [14], and sonochemical deposition [15], with different geometrical shapes and

NANOINNOVATION 2018
AIP Conf. Proc. 2145, 020005-1–020005-12; https://doi.org/10.1063/1.5123566
Published by AIP Publishing. 978-0-7354-1890-5/$30.00

structures. Among them anodization is a low cost and versatile method for production of porous or tubular nanostructures of highly ordered metal oxides which can significantly enhance the surface area without increasing the geometric area of materials [16]. Titania nanotubes (TiO_2 NTs) are typically synthetized through "double-step" anodization in acidified aqueous solutions containing a fluoride salt [17]. These nanotubes have diameters in the range of 60–150 nm, determined by the anodization potential and fluoride concentration while the length of the nanotubes is tailored by the anodization time [18]. The "double-step" anodization method consists of a first anodization of the titanium substrate at the end of which the TiO_2 layer is selectively removed and then a second anodization step take place. The removal of the first formed oxide gives an imprinting to the substrate surface which promote a highly ordered growth of the titania layer during the second anodization (Fig. 1). Several works studied the effects of fluoride concentration and water content in different organic electrolytes[19], paying attention to the formation of the so called "nano-grass" top tubes morphology, were the collapse of the top tubes takes place after the thinning of the walls due to chemical etching effect of the same anodization solution in fluoride containing electrolytes [17, 20].

In this work a facile "one-step" anodization method was proposed (Fig. 1), varying NH_4F/H_2O concentration ratios in ethylene glycol based electrolytes for different anodization times, in order to achieve a free nano-grass morphology. The so produced electrodes were then employed as substrates for the Cu_2O deposition.

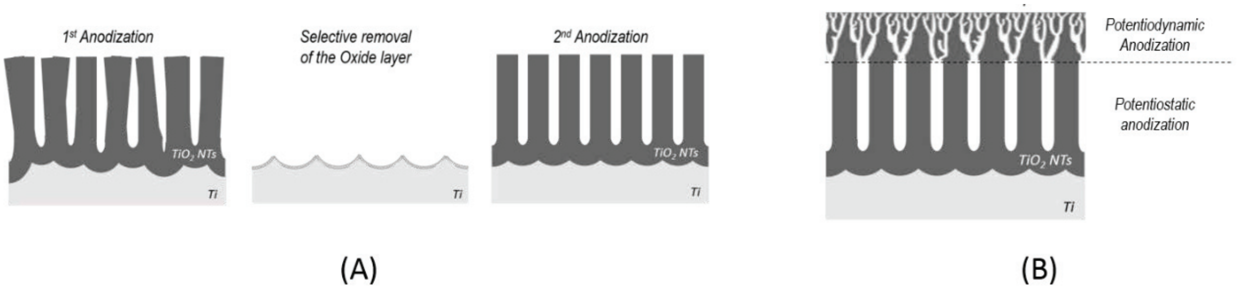

FIGURE 1. Schematic representation of the: A) typical "Double-step" anodization; B) "Single-step" anodization proposed in this work.

Traditionally, Cu_2O deposition techniques include the impregnation of nanostructured TiO_2 with a copper salt and subsequent calcination. These methods offer low control on deposited particles (e.g.: size, shape, composition), which mainly determines the TiO_2-Cu_2O activity [21]. Electrochemical deposition [16] of Cu_2O thin films is one of the most versatile and cost effective methods to deposit semiconductor nanoparticles over titania nanotubes [22]. A particularly attractive feature of electrodeposition is its ability to control size, shape and morphology of the deposited Cu_2O, which can significantly affect its electrical properties and the catalyst activity, by the appropriate control of its operating conditions [23–26]. The electrodeposition of Cu_2O nanoparticles (NPs) over Ti/TiO_2 NTs electrodes was investigated using a pulsed potential technique [27] in alkaline copper lactate electrolyte [28, 29].

MATERIALS AND METHODS

"Single-step" Anodization

The anodization process was carried out using titanium planar electrodes (Alfa Aesar 99.5%, annealed, thickness 0.25mm) in Ethylene Glycol (Alfa Aesar, 99+%) based electrolytes, varying NH_4F (Alfa Aesar, 98% min.) and H_2O content, following the concentrations ratio reported in Table 1. The two-electrodes jacketed cell is symmetric, both electrodes were titanium, kept at room temperature (24.5 ± 0.5)°C and magnetically stirred. The anodization process was conducted connecting the cell with a power supply (Aim-TTi CPX200DP DC Power Supply Dual Outputs, 2 x 60V/10A 180W). Prior to anodization, the titanium electrodes were pretreated just by Acetone (VWR Prolabo Chemicals, 100%) ultrasonic bath (Elma® S 10 Elmasonic, 220-240V∼, 30W, 50-60Hz), in order to degrease the titanium electrodes surface.

TABLE 1. NH_4F and H_2O Concentration Ratios in Different Ethylen Glycol Based Electrolytes.

Electrolyte	NH_4F [$\%_{wt}$]	H_2O [$\%_{v/v}$]
EG1	0.1	0.5
EG2	0.1	1.0
EG3	0.1	2.0
EG4	0.3	0.5
EG5	0.3	1.0
EG6	0.3	2.0

The applied potential (U) was imposed according two stages: a first linear growth (potentiodynamic anodization) up to 60V, reached which, it remains constant for different total durations (potentiostatic anodization), as reported in Table 2.

TABLE 2. Anodization Methods (AM).

Method	U Growth Rate [V/s]	U [V]	time [min]
AM1	0.5	60	17
AM2	0.5	60	32
AM3	0.5	60	62
AM4	0.5	60	92
AM5	0.5	60	122

At the end of the anodizations the electrodes were washed with acetone and then dried at least 24 h. In relation to the specific electrolyte and anodization time employed, after drying, a sonication treatment in distilled water was performed to achieve a free nano-grass surface.

Annealing treatment

The as formed titania NTs array resulting from anodization is amorphous. An annealing treatment was performed in a muffle furnace (Nabertherm B410, Tmax1100°C, 1.2KW), where the constant temperature of the specific treatment (T_A) is reached with a heating rate of 8°C min^{-1}. At the end of the constant temperature period the samples were immediately cooled out of the furnace at ambient temperature. The experimental conditions of the different annealing treatment tested are summarized in Table 3.

TABLE 3. Annealing Methods (AN).

Method	T_A Growth Rate [°C/min]	T_A [°C]	time [min]
AN1	8.0	580	132.5
AN2	8.0	680	145.0
AN3	8.0	580	252.5
AN4	8.0	680	265.0

Cu_2O Electrodeposition

The electrodeposition tests were performed in a three electrodes jacketed cell, magnetically stirred and kept at room temperature. Ti/TiO2 electrodes were employed as working electrode, a platinum gauze (Alfa Aesar 25 x 25 mm, 100 mesh woven from 0.0762 dia wire, 99.9% metal basis) was used as counter electrode, while an Ag/AgCl saturated electrode was the reference electrode. The applied potential values in electrodeposition tests reported in this work are referred to this latter reference electrode. The electrolyte is composed by CuSO4 0.4M in Lactic Acid 3M, and then pH is adjusted to 11.0 by the addiction of NaOH 5M. The electrodeposition tests were carried out with an IVIUMnSTAT potentiostat, following pulsed electrodeposition method based on the cyclic application of a first cathodic pulse (A period, t_{on}) followed by a zero-current time (B period, t_{off}), as reported in Table 4.

TABLE 4. Pulsed Electrodeposition Methods. E_A is the electrode potential during the A period, t_{on} is the duration of the A period, I_B is the imposed current during the B period, t_{off} is the duration of the B period.

Method	E_A [V]	t_{on} [s]	I_B [mA]	t_{off} [s]
PED1	-0.6	0.5	0	5
PED2	-0.8	0.5	0	5
PED3	-0.9	0.5	0	5

In any test, the duration of the electrodeposition was indirectly fixed by assigning the overall charge to be transferred (Q). For each electrodeposition method 3 different amount of transferred charge was set: 100mC, 400mC and 1200mC.

Characterizations of the Electrodes

Morphological characterization of the electrodes was performed by a field emission scanning electron microscopy (FE-SEM Zeiss Auriga). The software ImageJ was used to analyze FE-SEM images. Optical properties of the composite semiconductor based electrodes were investigated through Diffuse Reflectance Spectroscopy (KONICA MINOLTA CM-2600d Spectrophotometer), in the wavelength range 360 - 740 nm. X-ray diffractometer (Bruker D8 ADVANCE) with a Molybdenum anode ($K\alpha$ = 0.71Å) was employed for the crystal phases identification of the Ti/TiO_2 electrodes before and after the annealing treatment and the Cu_2O deposition. The diffractometer has a Bragg-Brentano focusing geometry which makes it suitable for thin films analysis using a reflection configuration.

RESULTS AND DISCUSSION

"Single-step" Anodization: Structural and Morphological Properties of the Ti/TiO_2 Electrodes

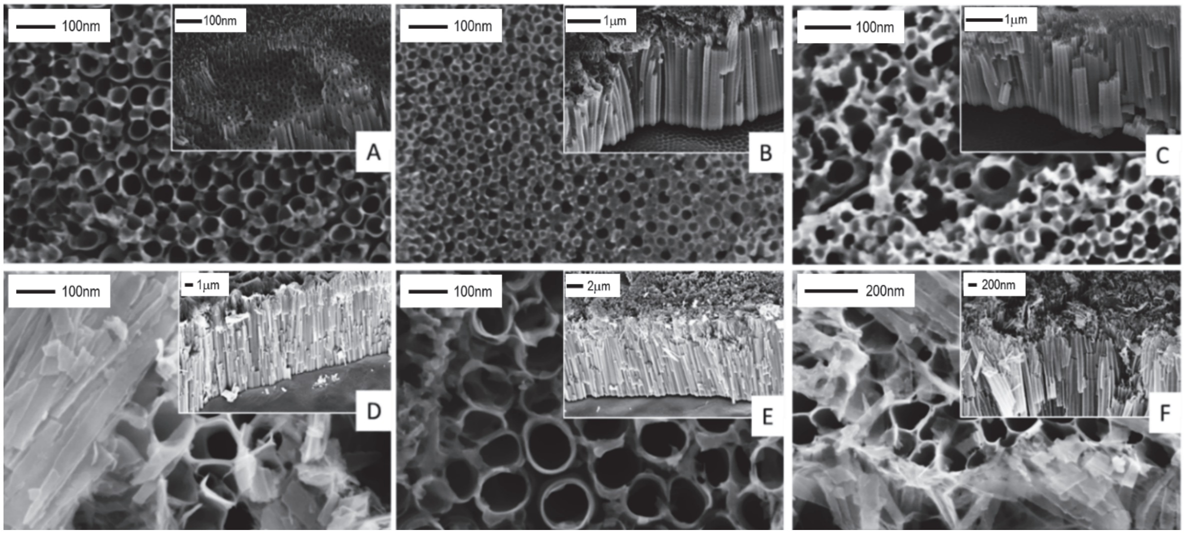

FIGURE 2. FE-SEM images, Ti/TiO2 electrodes as anodized (60V; 122 min.) in different EG based electrolytes: A) EG1, 0.1%$_{wt}$ NH_4F – 0.5%$_{v/v}$ H_2O; B) EG2, 0.1%$_{wt}$ NH_4F – 1.0%$_{v/v}$ H_2O; C) EG3, 0.1%$_{wt}$ NH_4F – 2.0%$_{v/v}$ H_2O; D) EG4, 0.3%$_{wt}$ NH_4F –0.5%$_{v/v}$ H_2O; E) EG5, 0.3%$_{wt}$ NH_4F – 1.0%$_{v/v}$ H_2O; F) EG6, 0.3%$_{wt}$ NH_4F – 2.0%$_{v/v}$ H_2O. The insets show the corresponding cross-sectional FE-SEM images.

The tuning of the anodization parameters is a crucial factor for the resulting structural and morphological properties of the TiO_2 NTs array [17, 22]. Figure 2 shows FE-SEM images of TiO_2 NTs grown at 60V for 122 min (AM5), in the different EG based electrolytes reported in Table 1. The same images have been used in NTs diameter estimation. Outer and inner tubes diameters have been compared to evaluate the effect of the parameters which mainly determine the structural properties of the TiO_2 NTs array, i.e. the applied potential and the composition of the electrolyte.

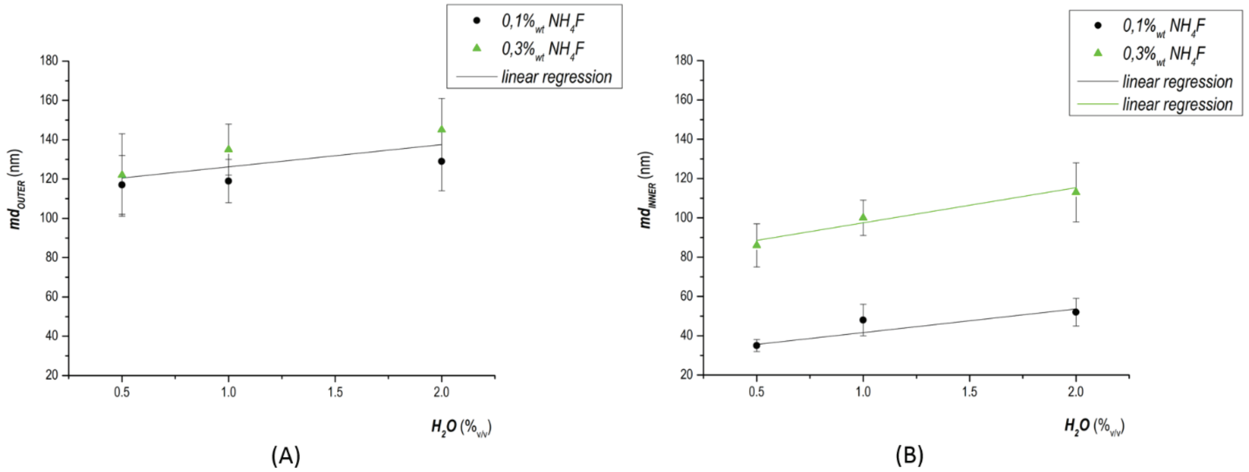

FIGURE 3. Mean diameter as a function of electrolyte concentration ratios. A) Outer tubes diameter (md_{OUTER}); B) Inner tubes diameter (md_{INNER}). In both diagrams the black circles correspond to $0.1\%_{wt}$ NH_4F while the green triangle to $0.3\%_{wt}$ NH_4F.

There aren't significative statistical differences ($p < 0.05\%$) in mean outer diameters varying with electrolyte's NH_4F content (Fig.3-A). On the contrary, at the same significance level the comparison about inner mean diameters (Fig.3-B), shows a significative difference between the two different NH_4F concentrations.

TABLE 5. Effect of Electrolyte Concentration Ratios on tubes diameter. *md* is the mean diameter and *s* the relative standard deviation.

Electrolyte	md_{OUTER} [nm]	s [nm]	md_{INNER} [nm]	s [nm]
EG1	122	21	35	3
EG2	135	13	48	8
EG3	145	16	52	7
EG4	117	15	86	11
EG5	119	11	100	9
EG6	129	15	113	15

From these evidences it is possible to assume that, unlike the external average diameter, the average internal diameter is significantly influenced by the electrolyte concentration ratios. Indeed, the etching effect due to the presence of fluorides in the electrolyte on the oxide already formed is well known [33]. We notice that, in accordance with previous literature studies [29, 30], the external average diameter can be effectively modified by varying the applied anodization potential (which is here maintained constant at 60 V). This effect, as function of the fluoride content, is confirmed by the top tube morphology (Fig. 2). The "single step" anodization method developed follows a potentiodynamic trend in its initial phase, where the formed oxide layer is characterized by a tree-like structure (Fig.1-B), below which the ordered growth of the nanotubes proceeds during the potentiostatic phase. The layer characterized by tree-like morphology (Fig.2-A, B, C), is no longer present when the fluoride content increases (Fig.2-D, E, F). Here the etching effect results in the formation of the unwanted nanograss layer, which consists in the thinning and consequent collapse of the walls of the nanotubes on the top of the oxide layer. Hence the fluoride concentration increase corresponds to an increased etching effect, which is useful to justify how the inner diameter of the nanotubes is mainly function of the electrolyte concentration ratios rather than the applied potential.

In relation to the thickness of the oxide layer the effect of the fluoride content is different: once the duration of anodization is fixed, as the fluoride concentration increases the thickness increases (data not shown), while for a fixed concentration, increasing the duration the etching effect becomes preponderant and there is a decrease in the growth coefficient, as shown in Fig.4. Consequently, the thickness of the oxide layer and the internal diameter of the nanotubes are dependent of both, fluoride concentration and anodization duration.

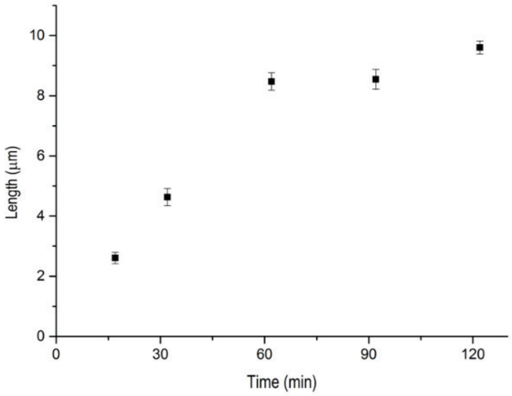

FIGURE 4. NTs growth rate in EG5 electrolyte at 60V.

Figure 4 shows the length of samples obtained in EG5 electrolyte at 60V for different anodization times (Table 2). The change in the growth rate of the NTs is evident after 1 hour of anodization, when the oxide dissolution rate becomes greater than the oxide growth rate (nanograss formation).

In order to achieve a free nano-grass surface (Fig.5-B), a sonication post-treatment was optimized for the electrodes obtained in EG5 electrolyte at 60V and 62min (AM3).

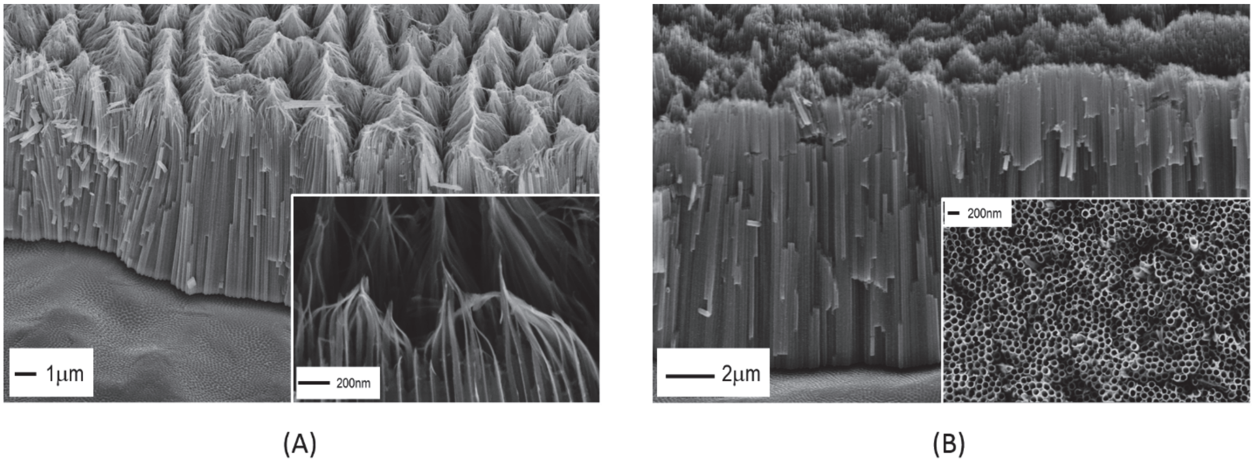

FIGURE 5. FE-SEM images - A) Cross sectional view, nano-grass layer on sample anodized in EG5 electrolyte at 60V (AM3); the inlet is a magnification of the collapsed top tubes. B) Cross sectional view, free nano-grass morphology in sample anodized in EG5 electrolyte at 60V (AM3) after sonication post-treatment; the inlet is a top view of the same sample.

Annealing Treatment Effect on Crystal Phases Ratio

At the end of the anodization process the titanium dioxide NTs array is amorphous, so an annealing treatment is needed to transform it in its crystal phases, i.e. Rutile and Anatase. The treatment was performed on sonicated Ti/TiO_2 electrodes obtained by anodization AM3 in EG5 electrolyte. The samples resulting from the different annealing treatment (Table 3) were characterized through XRD analysis and the relative diffractogram are showed in Fig. 6.

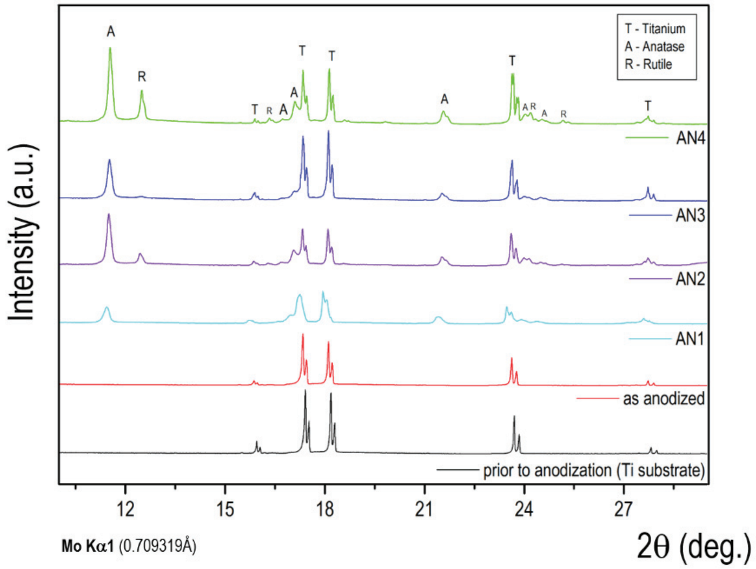

FIGURE 6. XRD patterns: Titanium electrode prior to anodization (black line); Ti/TiO_2 electrode after anodization (red line); Ti/TiO_2 electrode after annealing treatment AN3 performed at 580°C for 3h (blue line); Ti/TiO_2 electrode after annealing treatment AN4 performed at 680°C for 3h (green line).

The Rutile/Anatase ratio in the samples was determined according to the method described by Ding et al. [35]:

$$\%Rutile = \frac{1}{\left[1+0.8\cdot\left({}^{I_A}/_{I_R}\right)\right]}\cdot 100 \tag{1}$$

where I_A and I_R are the integrated intensity of Anatase (011) and Rutile (101), which are at about 2θ = 11.5° and 2θ = 12.5° respectively.

TABLE 6. Effect of Annealing treatment on the crystal phases Ratios.

Method	I_A	I_R	I_A/I_R	%Rutile
AN1	5795	---	---	---
AN2	23078	4990	4.6	21.3
AN3	24412	873	28.0	4.3
AN4	48833	19883	2.4	33.7

As reported in Table 6 the rutile percentage increase with the temperature and duration. For the treatment AN1 the percentage of rutile could not be estimated for the absence of a significative intensity of the (101) rutile peak. For that sample, it is possible to assume that the crystal phase is almost exclusively Anatase (*%Rutile < 4.3%*), which is the most photoactive phase [34].

Cu_2O Electrodeposition on Ti/TiO_2 Electrodes

The electrodeposition tests reported here were carried out using as working electrode the Ti/TiO_2 electrodes obtained by anodization in EG5 electrolyte and annealing treatment AN1. In order to evaluate the potential range for the Cu_2O reduction over Ti/TiO_2 electrodes a linear sweep voltammetry (LSV) was performed. The range investigated is between 0 and -1.2V (Vs Ag/AgCl) at a scan rate of 10 mV·s^{-1}. The Cu_2O reduction corresponds to the cathodic current peak in Fig.7-A, while the current starts to increase around a potential value of -0.4V. This is why the potentials set in the electrodeposition experiment (Table 4) are included in this latter range. A first evidence derives from the comparison between the morphology obtained for the different electrodeposition potential, as the FE-SEM images show (Fig.7-B,C) a morphological transition is observed, from octahedral to spherical Cu_2O NPs, from less to more cathodic electrodeposition potential respectively. While an increase in the amount of transferred charge corresponds to an increase in Cu_2O NPs sizes (Fig.8).

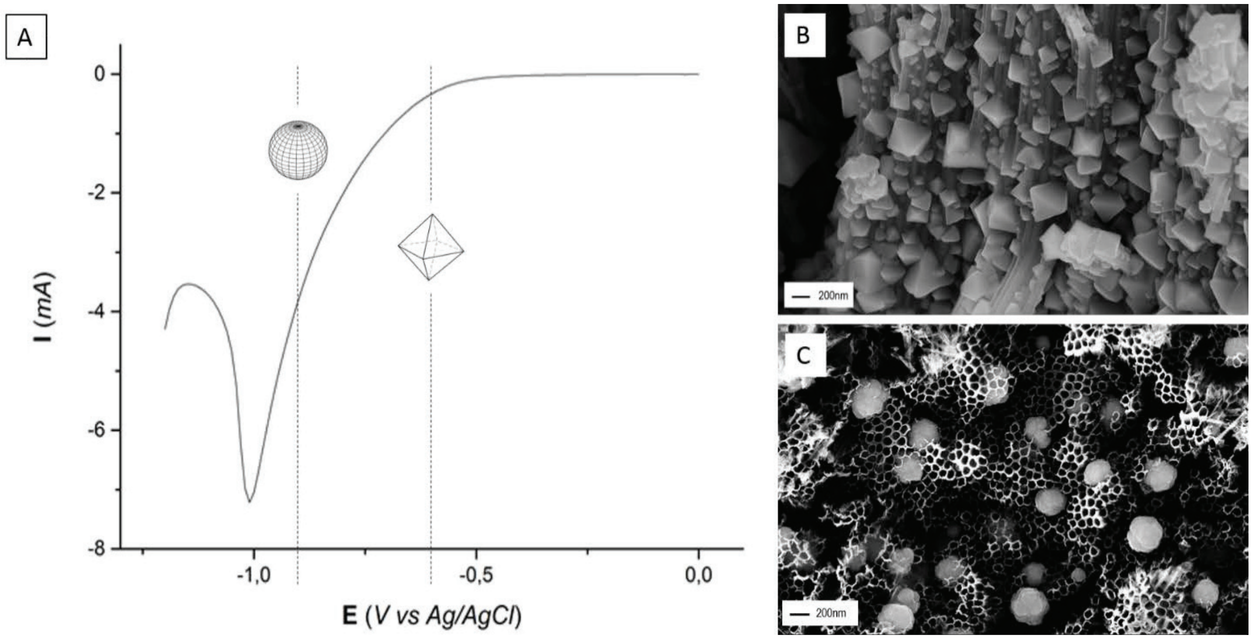

FIGURE 7. A) Linear sweep voltammetry of Ti/TiO_2 Electrode in electrodeposition solution ($CuSO_4$ 0.4M, Lactic Acid 3M, pH 11 - that concentrations are referred at the electrolyte before adjusting pH), scan rate 10 mV/s; B) FE-SEM images PED1, 1200mC of transferred charge (cross sectional view); C) FE-SEM images PED3, 1200mC of transferred charge (top view).

XRD analysis performed on the composite electrodes have been compared with the bare Ti/TiO_2 electrode (annealed AN1) (Fig.9). All the composite electrodes show the appearance of new peaks attributable to Cu_2O NPs and no differences are highlighted between the composite electrodes synthetized varying the electrodeposition method.

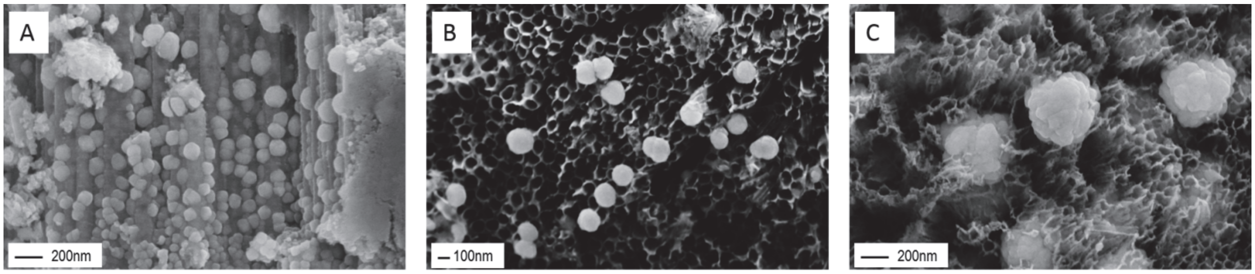

FIGURE 8. FE-SEM images PED3: A) 100mC (cross sectional view); B) 400mC (top view); C) 1200mC (top view).

Optical Characterization of the Electrodes

Diffuse Reflectance Spectroscopy (DRS) was employed for the optical properties of the semiconductor-based electrodes characterization, i.e. energy band gap estimation. Two methods have been employed, a simple method according to Radecka et al. [36], which can be applied directly to the Reflectance curve, plotting its first derivative $(dR/d\lambda)$ as a function of the wavelength (λ), (red dots, Fig.10-A).

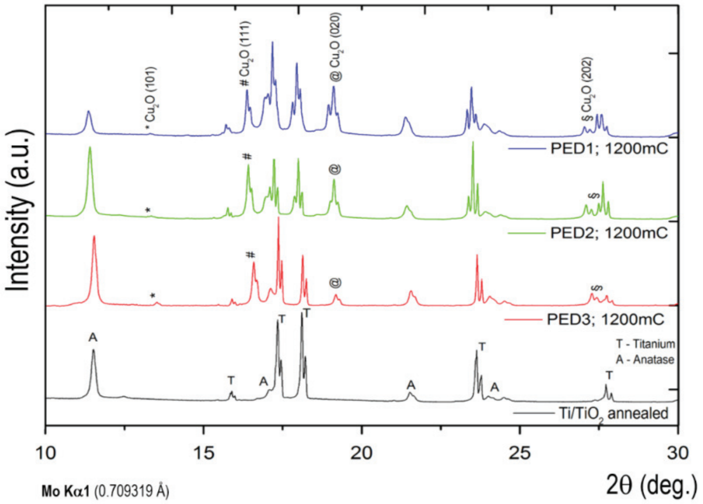

FIGURE 9. XRD patterns of the composite Ti/TiO$_2$/Cu$_2$O Electrodes: PED1, 1200mC of transferred charge (blue line); PED2, 1200mC of transferred charge (green line); PED3, 1200mC of transferred charge (red line). The black line is the XRD pattern of Ti/TiO$_2$ electrode annealed (AN3).

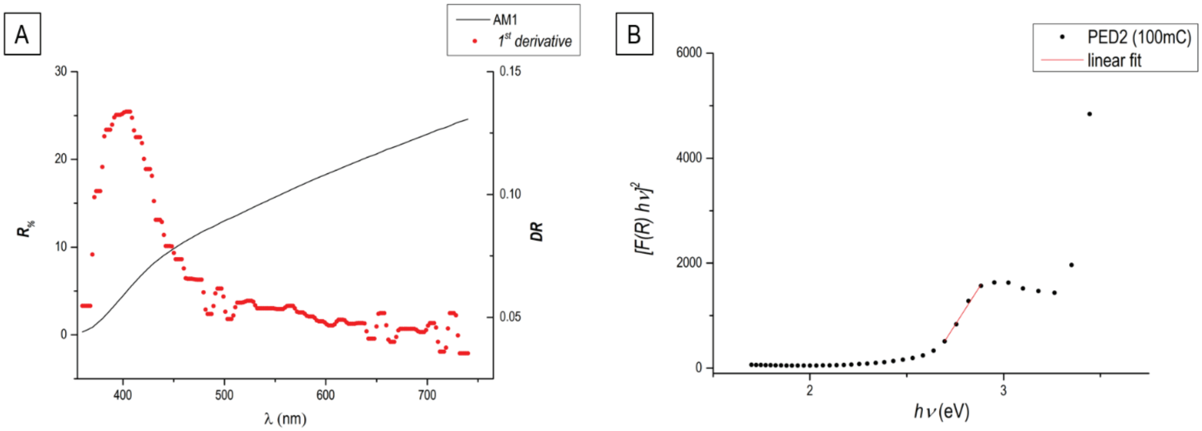

FIGURE 10. Energy band gap estimation from DRS spectra: A) Radecka method, Reflectance spectrum (black line) and its 1st derivative (red dots), obtained for Ti/TiO$_2$ electrode as anodized (AM1, EG5 electrolyte); B) Transformed equivalent absorption product ($[F(R_\infty)\cdot h\nu]^{1/n}$) for n = 1/2 (black dots) and straight intercept (linear section of the curve) with energy axes (red line), obtained for composite Ti/TiO$_2$/Cu$_2$O electrode (PED2, 100mC).

The band gap is calculated substituting the wavelength related to the maximum point of the differential reflectance curve in the equation (2):

$$E_g = \frac{hc}{\lambda} \tag{2}$$

where h is the Plank's constant and c is the speed of light. The other is the Tauc plot method [37]. It assumes that the absorption coefficient (α) is related to the energy band gap (E_g) by the following equation:

$$\alpha h\nu = A\left(h\nu - E_g\right)^n \tag{3}$$

where A is a proportionality constant and n is a power index related to the electronical transition, which may assumes the values 1/2 or 3/2 for direct electronic transition, allowed and forbidden respectively; and 2 or 3 for indirect electronic transition, allowed and forbidden respectively [38]. The method is based on a plot of $(\alpha h\nu)^{1/n}$ as a function of photon energy $h\nu$, where the energy band gap is estimated extrapolating the intercept between the linear part of the plot and the photon energy axis.

Reflectance can be converted into the equivalent absorption coefficient, α, according to the Kubelka-Munk (K-M) theory [28, 29]:

$$F(R_\infty) = \frac{(1-R_\infty)^2}{2R_\infty} = \frac{k(\lambda)}{S(\lambda)} \sim \alpha \tag{4}$$

where $F(R_\infty)$ is the so called K–M function, $R_\infty = R_{sample}/R_{standard}$, $k(\lambda)$ is the absorption coefficient and $S(\lambda)$ is the scattering coefficient for the measured sample [41]. Considering S as wavelength independent, the K-M function ($F(R_\infty)$) is approximately proportional to the absorption coefficient (α) and the Equation (3) becomes:

$$[F(R_\infty) \cdot h\nu]^{1/n} = A\left(h\nu - E_g\right) \tag{5}$$

As reported from Wang et al. [42], it is well established that bulk Cu_2O has a direct optically allowed band gap of 2.62 eV.

TABLE 7. Cu_2O energy band gap estimation in composite $Ti/TiO_2/Cu_2O$ electrodes. $E_{g,R}$ energy band gap estimated by Radecka method; $E_{g,T}$ energy band gap estimated by Tauc plot method for *n = 1/2* (direct optical allowed band gap).

Method	$E_{g,R}$ [eV]	s [eV]	$E_{g,T}$ [eV], n=1/2	s [eV]
PED1	2.58	0.03	2.53	0.04
PED2	2.60	0.05	2.56	0.06
PED3	2.58	0.03	2.55	0.03

In Table 7 are summarized the Energy band gaps estimated for Cu_2O in composite $Ti/TiO_2/Cu_2O$ electrodes with the two methods described above. The estimated values for the composite electrodes correspond to an absorption in the visible region (λ > 400nm), confirming the improved absorption characteristics of the composite electrodes respect to the bare TiO_2 electrode which doesn't exhibit absorption in visible region (Fig.11).

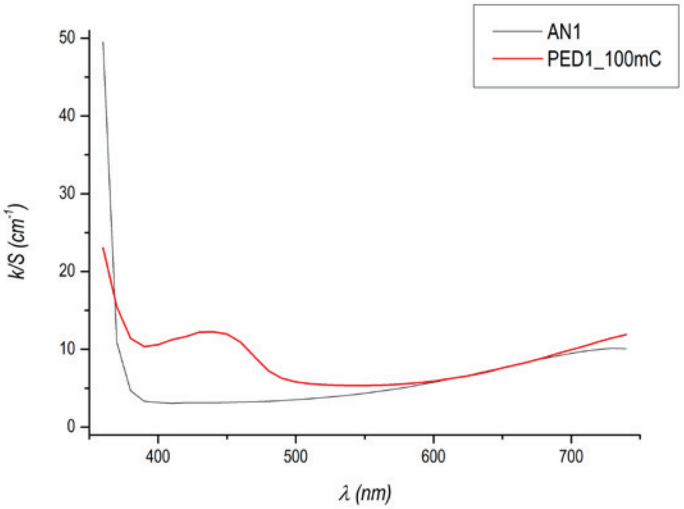

FIGURE 11. Equivalent absorption spetra from DRS analysis for Ti/TiO_2 annealed (AN1, black line) and composite $Ti/TiO_2/Cu_2O$ (PED1_100mC, red line)

CONCLUSIONS

Facile “Single-step” anodization method was developed for Ti/TiO_2 electrodes production with highly ordered NTs array. The influence of annealing temperature and duration for TiO2 transformation in its crystal phases (Anatase and Rutile) was also evaluated. Anatase Ti/TiO_2 NTs electrodes (Rutile < 4%) were then used as working electrodes in electrodeposition of Cu_2O NPs through a pulsed potentiostatic technique. Morphology of NPs were influenced by the imposed potential and the average size of NPs has been controlled increasing the amount of the overall transferred charge. Optical characterization confirmed that composite electrodes shows energy band gaps which make them suitable for visible light absorption, allowing so to overcome the limits of the bare TiO_2 electrodes (UV-light absorption), enabling their improved use for photo-electrochemical and photo-catalytic applications.

ACNOWLEGMENTS

The authors greatly acknowledge the Centre for Nanotechnology Applied to Engineering (CNIS nanolab) of Sapienza University of Rome for the FE-SEM and XRD analysis.

REFERENCES

1. Lu, Q. & Jiao, F. *Nano Energy* **29**, 439–456 (2016).
2. Momirlan, M. & Veziroglu, T. N. *Int. J. Hydrogen Energy* **30**, 795–802 (2005).
3. Wang, D. *et al. Electrochim. Acta* **130**, 290–295 (2014).
4. Tran, N. H. & Kannangara, G. S. K. *Chem. Soc. Rev.* **42**, 9454–9479 (2013).
5. Holladay, J. D., Hu, J., King, D. L. & Wang, Y. *Catal. Today* **139**, 244–260 (2009).
6. Sun, Y., Wang, G. & Yan, K. *Int. J. Hydrogen Energy* **36**, 15502–15508 (2011).
7. Paola, A. Di *et al. Catal. Today* **75**, 87–93 (2002).
8. Lei, L., Su, Y., Zhou, M., Zhang, X. & Chen, X. *Mater. Res. Bull.* **42**, 2230–2236 (2007).
9. Wang, M., Ioccozia, J., Sun, L., Lin, C. & Lin, Z. *Energy Environ. Sci.* **7**, 2182–2202 (2014).
10. Janczarek, M. & Kowalska, E. *Catalysts* **7**, 317 (2017).
11. Clarizia, L. *et al. Int. J. Hydrogen Energy* **39**, 16812–16831 (2014).
12. Nakajima, A., Nakamura, A., Arimitsu, N., Kameshima, Y. & Okada, K. *Thin Solid Films* **516**, 6392–6397 (2008).
13. Taveira, L. V., Macák, J. M., Tsuchiya, H., Dick, L. F. P. & Schmuki, P. *J. Electrochem. Soc.* **152**, B405 (2005).
14. Ikraam, M., Shahid, S., Zaman, S. & Sarwar, M. N. *J. Electron. Mater.* **45**, 4228–4236 (2016).
15. R. Vijaya Kumar, Y. Diamant, and & Gedanken*, A. (2000). doi:10.1021/CM000166Z
16. Schiavi, P. G., Altimari, P., Rubino, A. & Pagnanelli, F. *Electrochim. Acta* **259**, 711–722 (2018).
17. Mir, N., Lee, K., Paramasivam, I. & Schmuki, P. *Chem. - A Eur. J.* **18**, 11862–11866 (2012).
18. Raja, K. S., Gandhi, T. & Misra, M. *Electrochem. commun.* **9**, 1069–1076 (2007).
19. Albu, S. P. & Schmuki, P. *Phys. status solidi - Rapid Res. Lett.* **4**, 215–217 (2010).
20. Kim, D., Ghicov, A. & Schmuki, P. *Electrochem. commun.* **10**, 1835–1838 (2008).
21. Tsui, L. -k., Wu, L., Swami, N. & Zangari, G. *ECS Electrochem. Lett.* **1**, D15–D19 (2012).
22. Huang, L. *et al. Mater. Chem. Phys.* **130**, 316–322 (2011).
23. Altimari, P. & Pagnanelli, F. *Electrochim. Acta* **206**, 116–126 (2016).
24. Altimari, P. & Pagnanelli, F. *Electrochim. Acta* **205**, 113–117 (2016).
25. Schiavi, P. G., Altimari, P., Zanoni, R. & Pagnanelli, F. *Electrochim. Acta* **220**, 405–416 (2016).
26. Schiavi, P. G., Rubino, A., Altimari, P. & Pagnanelli, F. *AIP Conf. Proc.* **1990**, (2018).
27. Pagnanelli, F. *et al. Electrochim. Acta* **155**, 228–235 (2015).
28. Huang, L. *et al. Scr. Mater.* **63**, 159–161 (2010).
29. Zhang, S. *et al. Electrochem. commun.* **13**, 861–864 (2011).
30. Roy, P., Berger, S. & Schmuki, P. *Angew. Chemie - Int. Ed.* **50**, 2904–2939 (2011).
31. Macak, J. M. *et al.* **11**, 3–18 (2007).
32. Schultze JW, L. M. **45**, 2499–2513 (2000).
33. Roy, P., Berger, S. & Schmuki, P. *Angew. Chemie Int. Ed.* **50**, 2904–2939 (2011).

34. Sreekantan, S., Hazan, R. & Lockman, Z. *Thin Solid Films* **518**, 16–21 (2009).
35. Ding, X. Z., Liu, X. H. & He, Y. Z. *J. Mater. Sci. Lett.* **15**, 1789–1791 (1996).
36. Radecka, M. *et al.* *J. Nanosci. Nanotechnol.* **10**, 1032–1042 (2010).
37. Tauc, J. *Mater. Res. Bull.* **5**, 721–729 (1970).
38. Michalow, K. A. *et al.* *Catal. Today* **144**, 7–12 (2009).
39. Kubelka, P. *J. Opt. Soc. Am.* **38**, 1067 (1948).
40. Džimbeg-Malčić, V., Barbarić-Mikočević, Ž. & Itrić, K. **1**, 117–124 (2011).
41. Torrent, J. & Barron, V. *Encycl. Surf. Colloid Sci.* 1438–1446 (2002). doi:10.1081/E-ESCS3-120000047
42. Wang, Y. *et al.* *Phys. Rev. B* **94**, (2016).